Charactering Catalytic Ignition and Combustion for the Ninety-Percent Hydrogen-Peroxide/Paraffin-Based Hybrid Rocket Engine

Zezhong Wang,* Xin Lin,† Kun Wu,‡ Zelin Zhang,§ Sihan Fang,¶
Dongdong Meng,** Fei Li,†† and Xilong Yu††
State Key Laboratory of High Temperature Gas Dynamics, Chinese Academy of Sciences, 100190
Beijing, People's Republic of China

The present work performed a combined experimental and numerical investigation of the catalytic ignition and combustion characteristics for a hybrid rocket engine (HRE) using 90% hydrogen peroxide (H_2O_2) with a paraffin-based fuel as the propellant system. The variation of the H_2O_2 decomposition temperature used as the analytical premise was monitored by a thermocouple and laser absorption spectroscopy based on water absorption. The effects of preheating, the number of silver mesh layers, and the usage count for the catalytic bed on the H_2O_2 decomposition characteristics were analyzed. A preheated 60-layer silver catalyst bed provided the best decomposition performance, including the shortest catalytic decomposition delay time and the highest decomposition efficiency. A two-dimensional numerical model was built to determine the effect of decomposition efficiency decay on the HRE combustion characteristics. Variations in the combustion temperature, combustion chamber pressure, and product distribution were compared for H_2O_2 decomposition efficiencies ranging from 70 to 100%. As the decomposition efficiency of H_2O_2 decreased to 80%, part of the oxidizer was blown out the chamber before participating in the combustion, yielding a significant decline in the combustion performance of the hybrid rocket engine. Static firing tests were also used to determine the catalytic ignition and reignition performance of the HRE. The results showed that the performance of the catalytic bed was stable while the reignition process was rapid without a pressure peak.

Nomenclature

A	=	integrated absorbance
C_p	=	specific heat capacity
c	=	speed of light
D	=	diameter
E	=	energy
E''	=	low-state energy
e	=	measurement error
G_{ox}	=	oxidizer mass flux
H_D	=	decomposition enthalpy
H_V	=	latent heat of evaporation
h_P	=	Planck's constant
I_0	=	incident laser intensity
I_t	=	transmitted laser intensity
k	=	turbulent kinetic energy
k_B	=	Boltzmann's constant
k_v	=	spectral absorption coefficient
L	=	path length
M_{H_2O}	=	molar mass of water
$\dot{m}$	=	mass flow rate
P, p	=	pressure
P_x	=	partial pressure
$Q(T)$	=	partition function of the absorbing molecule
Q_a	=	heat of absorption
Q_d	=	heat of decomposition
R	=	ideal gas constant
$S(T)$	=	line strength of the transition at temperature T
T	=	temperature
t	=	burning time
u	=	velocity
V_g	=	outlet velocity
v	=	laser frequency
v_0	=	line center frequency
γ	=	ratio of specific heat capacity
ε	=	turbulence eddy dissipation
η	=	catalytic decomposition efficiency
μ	=	viscosity coefficient
ρ	=	density
σ^*	=	nozzle outlet area
$\phi(v)$	=	line shape function

Subscripts

i, j	=	tensor coordinates
ox	=	oxidizer
0, 1, 2	=	hydrogen peroxide, water, and oxygen, respectively

*Postdoctoral Student, Institute of Mechanics.
†Senior Engineer, Institute of Mechanics; linxin_bit@imech.ac.cn (Corresponding Author).
‡Associate Professor, Institute of Mechanics; wukun@imech.ac (Co-Corresponding Author).
§Master's Student, Institute of Mechanics.
¶Ph.D. Candidate, Institute of Mechanics.
**Engineer, Institute of Mechanics.
††Professor, Institute of Mechanics.

I. Introduction

THE continuous deployment of space technology worldwide has led to requirements for rocket engines that provide advantages such as low cost, safety, and minimal environmental impact along with adjustable thrust and multiple restart capabilities [1]. A hybrid rocket engine (HRE) typically employs a solid fuel together with a liquid oxidizer as the propellant system. Structures in which these propellant components are stored separately can allow the HRE to meet the requirements noted, and so these engines have potential applications in sounding rockets, launch vehicles, boosters, suborbital vehicles, and even ramjets [2,3].

Although the separate storage of propellant components provides HREs with the potential for multiple restarts, the stable and reliable implementation of restarts remains a challenge; and the associated technology is at an immature stage of development [4]. In particular, a suitable ignition method is an important prerequisite to achieving these goals, and catalytic ignition provides the advantages of simple structure, ready reignition, and the lack of a need for an additional

ignition propellant [5]. Even so, the catalytic ignition of an HRE is a complex process involving the decomposition of an oxidizer, heat exchange, melting, pyrolysis, mixing, and flame propagation. These processes are also affected by both the characteristics of the catalyst bed and by the propellant composition [6]. Therefore, more fundamental investigations of the catalytic ignition and reignition of HREs are necessary.

Hydrogen peroxide (H_2O_2) is a widely used oxidizer in the field of propulsion and provides various advantages, including minimal environmental impact, relatively easy storage, low toxicity, nontoxic combustion products, incompressibility, high density, and the capacity for catalytic decomposition. Consequently, H_2O_2 has been increasingly used as the oxidizer in studies concerning HREs [7,8]. As examples, Jang et al. [9] and Jo [10] investigated the characteristics of H_2O_2 decomposition in conjunction with different catalytic beds, whereas Connell et al. [11] and John et al. [12] explored the effects of trigger additions on the ignition characteristics of HREs. Yun et al. [13] and Whitmore et al. [14] carried out firing tests to examine the catalytic ignition characteristics and combustion performances of high-density polyethylene and acrylonitrile-butadiene-styrene fuels in conjunction with varying H_2O_2 concentrations. Cai et al. [15] and Tian et al. [16] established an ignition model for HREs and performed experimental and numerical analyses of the relationships between the ignition process and parameters such as the temperature, the oxygen/fuel (O/F) ratio, and the oxidizer mass flow rate.

However, additional research concerning the quantitative aspects of the catalytic decomposition of H_2O_2 is still required. This is partly because present day evaluation methods are primarily based on monitoring temperature and pressure changes [17]. This is unfortunate because internal single-point temperature measurements rarely capture the dynamic temperature changes associated with catalytic decomposition processes, especially in the case of reignition. Single-point measurements also do not accurately reflect the overall temperature distribution of the HRE. In addition, although a properly designed catalytic bed can achieve the complete decomposition of H_2O_2, the catalytic decomposition efficiency will inevitably decrease as the bed ages, especially during more complex reignition processes. This decrease in decomposition efficiency will, in turn, affect the combustion characteristics of the HRE.

Finally, the specific propellant combination will also affect the catalytic ignition of HREs. The high regression rates of liquefied paraffin-based substances resulting from droplet entrainment make these promising solid fuels [18–24]. However, there have been few studies regarding the catalytic ignition and reignition of paraffin-based fuels combined with H_2O_2 as the oxidizer. In particular, the ignition process of paraffin-based fuels may be affected by the extent to which the material is melted as a consequence of the low melting points of these fuels.

The present work conducted experimental and numerical assessments concerning the catalytic ignition and combustion of an HRE incorporating a H_2O_2/paraffin propellant system. These trials used four sets of catalytic beds having 20, 40, 60, or 80 layers of silver mesh. In addition to single-point temperature measurements using thermocouples, line-averaged dynamic temperature changes downstream of the catalytic bed were also monitored by employing laser absorption spectroscopy (LAS) with a 2.0 kHz repetition rate [25,26]. Based on the

substantial temperature data that were accumulated, the decomposition characteristics of H_2O_2 in these systems were evaluated; and the effects of preheating, the number of silver mesh layers, and the repeated use of the catalytic bed were all assessed. The relationships between the H_2O_2 decomposition efficiency and various combustion parameters (including combustion temperature, pressure, and distribution) were examined by establishing a two-dimensional numerical model of an HRE. Finally, firing tests were carried out using a laboratory-scale 90% H_2O_2/paraffin-based HRE to investigate the catalytic ignition and reignition in this system.

II. Methodology

A. Evaluating Catalytic Ignition Characteristics

Figure 1 provides a flowchart that summarizes the process used to evaluate catalytic ignition in the present work. Catalytic decomposition experiments with 90% H_2O_2 were initially carried out in conjunction with the silver catalyst bed. During these trials, thermocouples and LAS were simultaneously used to monitor the dynamic decomposition process. Based on the resulting data, the H_2O_2 decomposition temperature, delay time, and efficiency were evaluated while varying the extent of preheating, the number of silver mesh layers, and the number of bed usages. A two-dimensional numerical simulation was then conducted to analyze the combustion characteristics obtained with different H_2O_2 decomposition efficiencies. Finally, firing tests of an actual H_2O_2/paraffin HRE were carried out.

B. Laser Absorption Spectroscopy

The theory of direct absorption spectroscopy is briefly reviewed here [27–30]. In the case that a laser beam having a frequency v enters a uniform gaseous medium, some proportion of the laser light will be absorbed. According to the Beer–Lambert law, the proportional transmission of the laser beam intensity I_t/I_0 can be expressed as

$$\left(\frac{I_t}{I_0}\right)_v = \exp(-k_v L) \tag{1}$$

According to the preceding formula, the average temperature along the laser path can be calculated as

$$T = \frac{\dfrac{h_P c}{k_B}(E_2'' - E_1'')}{\ln\dfrac{A_1}{A_2} + \ln\dfrac{S_2(T_0)}{S_1(T_0)} + \dfrac{h_P c}{k_B}\dfrac{(E_2'' - E_1'')}{T_0}} \tag{2}$$

and the average partial pressure of the water vapor $P_{x_{H_2O}}$ can be obtained using the equation

$$P_{x_{H_2O}} = \frac{A}{S(T)L} \tag{3}$$

In the present work, the delay time associated with the catalytic decomposition of H_2O_2 could be directly obtained from the temperature data acquired using LAS. The process by which the H_2O_2 decomposition efficiency was evaluated based on the LAS data is
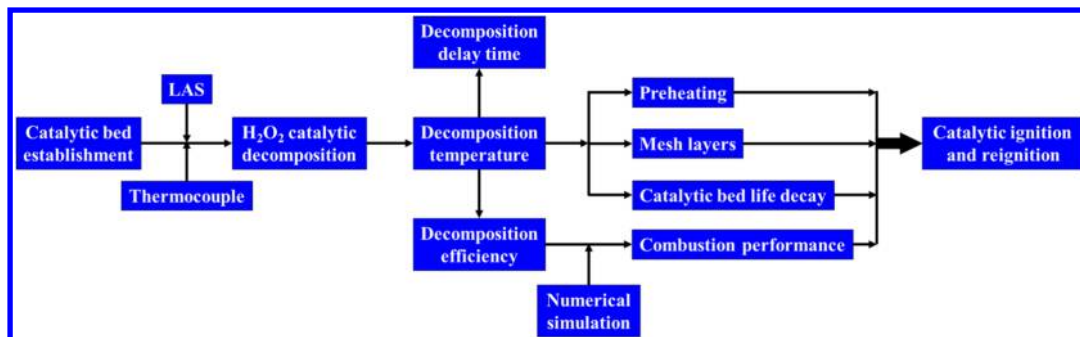

Fig. 1 The sequence of evaluations in the present work.

briefly introduced here, and further details can be found in previous work by Wang et al. [26]. Based on the ideal gas assumption, the parameters associated with the H_2O_2 decomposition product [water (H_2O)] will satisfy the equation

$$P_{x_{H_2O}} \sigma^* V_g = \frac{\dot{m}_{H_2O}}{M_{H_2O}} RT \quad (4)$$

The mass flow rate of the H_2O_2 was therefore calculated as

$$\dot{m}_{H_2O_2\_measured} = \frac{17}{9} \frac{P_{x_{H_2O}} \sigma^* V_g M_{H_2O}}{RT} - \frac{17}{81} \dot{m}_{H_2O_2\_consumed} \quad (5)$$

and so the H_2O_2 decomposition efficiency could be determined as

$$\eta = \frac{\dot{m}_{H_2O_2\_measured}}{\dot{m}_{H_2O_2\_consumed}} = \frac{17}{9} \frac{P_{x_{H_2O}} \sigma^* V_g M_{H_2O}}{RT \dot{m}_{H_2O_2\_consumed}} - \frac{17}{81} \quad (6)$$

C. Numerical Methodology

The HRE that was numerically modeled in this work is presented in Fig. 2a. The diameters of the precombustion chamber D_1, the fuel grain D_2, the postcombustion chamber D_3, the nozzle throat D_4, and the nozzle outlet D_5 were 30, 15, 50, 5, and 10 mm, respectively. The lengths of the precombustion chamber L_1, the fuel grain L_2, and the postcombustion chamber L_3 were 15, 62, and 53 mm, respectively. The downstream area of the injector panel was chosen as the calculation domain, and the corresponding two-dimensional asymmetric computational model is shown in Fig. 2b.

Considering the axisymmetric characteristics of the HRE, asymmetric two-dimensional simulations were performed. The numerical calculation was based on the compressible Reynolds-averaged Navier–Stokes equations with species transport:
    Continuity equation:

$$\frac{\partial \overline{\rho}}{\partial t} + \frac{\partial \overline{\rho} \tilde{u}_i}{\partial x_i} = 0 \quad (7)$$

Momentum equation:

$$\frac{\partial \overline{\rho} \tilde{u}_j}{\partial t} + \frac{\partial}{\partial x_i} (\overline{\rho} \tilde{u}_i \tilde{u}_j) = -\frac{\partial \overline{p}}{\partial x_j} + \frac{\partial}{\partial x} \left(\overline{\tau}_{ij} - \overline{\rho} \widetilde{u_i'' u_j''} \right) \quad (8)$$

Energy equation:

$$\frac{\partial \overline{\rho} \tilde{H}}{\partial t} + \frac{\partial}{\partial x_i} (\overline{\rho} \tilde{u}_i \tilde{H}) = \frac{\partial}{\partial x_i} \left(\frac{\overline{\lambda}}{\overline{c}_p} \frac{\partial \tilde{H}}{\partial x_i} - \overline{\rho} \widetilde{u_i'' H''} \right) \quad (9)$$
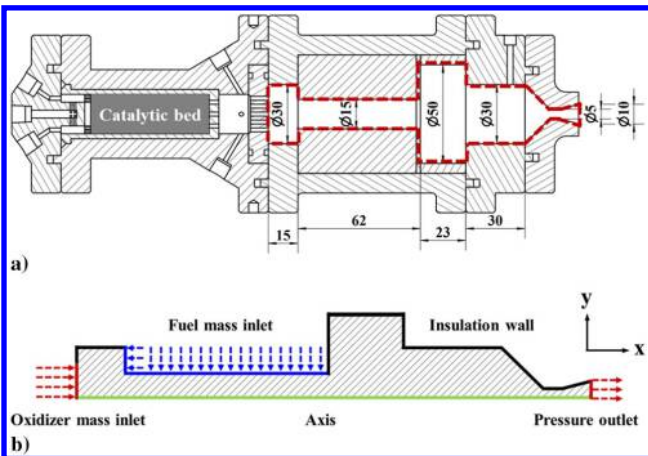

Fig. 2 Representations of a) the two-dimensional structure of the HRE used in this work and b) the asymmetric two-dimensional calculation domain.

Species transport equation:

$$\frac{\partial \overline{\rho} \tilde{Y}_k}{\partial t} + \frac{\partial}{\partial x_i} (\overline{\rho} \tilde{u}_i \tilde{Y}_k) = \frac{\partial}{\partial x_i} \left[\left(\rho D_{k,m} + \frac{\mu_t}{Sc_t} \right) \frac{\partial \tilde{Y}_k}{\partial x_i} \right] + \overline{\dot{\omega}}_k \quad (10)$$

where ρ, p, and u_i denote the density, pressure, and the velocity component in the i direction; u_i'' is the fluctuating component of velocity, whereas $^-$ and $\sim$ represent Reynolds and Favre averaging, respectively. The viscous stress tensor $\overline{\tau}_{ij}$ was given by

$$\overline{\tau}_{ij} = \mu \left(\frac{\partial \tilde{u}_i}{\partial x_j} + \frac{\partial \tilde{u}_j}{\partial x_i} - \frac{2}{3} \delta_{ij} \frac{\partial \tilde{u}_k}{\partial x_k} \right) \quad (11)$$

where μ is the dynamic viscosity. The total specific energy $\tilde{H}$ is defined by the sum of the static specific enthalpy $\tilde{h}$ and the specific kinetic energy $1/2 \tilde{u}_i \tilde{u}_i$, whereas c_p and λ are the specific heat capacity and the thermal conductivity of the mixture. NASA polynomials were implemented for the enthalpy and heat capacity of the individual species. The mixture values were calculated using a mass fraction weighted averaging among Ns species:

$$\tilde{h} = \sum_{k=1}^{Ns} \tilde{Y}_k \cdot \tilde{h}_k \qquad \overline{c}_p = \sum_{k=1}^{Ns} \tilde{Y}_k \cdot \tilde{c}_{p,k} \quad (12)$$

Thermodynamic closure was obtained by assuming a thermally perfect gas mixture governed by the equation of state

$$\overline{p} = \overline{\rho} R \tilde{T} \qquad \text{with } R = \sum_{k=1}^{Ns} Y_k R_k \quad (13)$$

where R_k is the species gas constant. The species viscosity and thermal conductivity of individual species were evaluated by the kinetic theory with the Lennard–Jones characteristic length and energy parameters. The mixture-averaged viscosity and thermal conductivity were obtained using the Wilke's law [31] and the combination averaging, respectively, whereas the mass diffusivities were obtained by assuming a constant Schmidt number of $Sc = 0.7$. We also noted that the flow in the combustor chamber was relatively slow with a Mach number sufficiently lower than 0.3, and therefore the work done by the viscous and turbulent stresses was not considered in the present simulation.

The turbulent closure of the unclosed terms introduced by the Reynolds averaging of the Navier–Stokes equation was achieved by invoking the Boussinesq hypothesis, which was modeled as

$$\overline{\rho} \widetilde{u_i'' u_j''} = -\mu_t \left(\frac{\partial \tilde{u}_i}{\partial x_j} + \frac{\partial \tilde{u}_j}{\partial x_i} - \frac{2}{3} \delta_{ij} \frac{\partial \tilde{u}_k}{\partial x_k} \right) + \frac{2}{3} \overline{\rho} k \quad (14)$$

in which μ_t is the turbulent viscosity, and k is the turbulent kinetic energy. Likewise, the turbulent heat flux in Eq. (9) can be modeled using the turbulent Prandtl number Pr_t:

$$\overline{\rho} \widetilde{u_i'' H''} = -\frac{\lambda_t}{\overline{c}_p} \frac{\partial \tilde{H}}{\partial x_i} = -\frac{\mu_t}{Pr_t} \frac{\partial \tilde{H}}{\partial x_i} \quad (15)$$

A constant Pr_t value equal to 0.9 was chosen for the present study as suggested by Riedmann et al. [32] for rocket combustor simulations; whereas for the turbulent mass diffusion in Eq. (10), a turbulent Schmidt number of $Sc_t = 0.7$ was adopted. To evaluate the turbulent viscosity, the realizable $k - \varepsilon$ turbulence model [33] was employed in the present work, in which two additional transport equations of the turbulent kinetic energy k and its dissipation rate ε were solved:

$$\frac{\partial}{\partial t} (\rho k) + \frac{\partial}{\partial x_j} (\rho k u_j) = \frac{\partial}{\partial x_j} \left[\left(\mu + \frac{\mu_t}{\sigma_k} \right) \frac{\partial k}{\partial x_j} \right] + \mu_t \tilde{S}^2 - \rho \varepsilon \quad (16)$$

$$\frac{\partial}{\partial t} (\rho \varepsilon) + \frac{\partial}{\partial x_j} (\rho \varepsilon u_j) = \frac{\partial}{\partial x_j} \left[\left(\mu + \frac{\mu_t}{\sigma_\varepsilon} \right) \frac{\partial \varepsilon}{\partial x_j} \right] + \rho C_1 \tilde{S} \varepsilon - \rho C_2 \frac{\varepsilon^2}{k + \sqrt{\nu \varepsilon}}$$

$$(17)$$

where $\sigma_k = 1.0$ and $\sigma_e = 1.2$ are the Prandtl numbers for k and ε, respectively; and $\tilde{S} = \sqrt{2S_{ij}S_{ij}}$ denotes the modulus of the rate-of-strain tensor. For the model constants, $C_1 = \max[0.43, \eta/(\eta + 5)]$ with $\eta = \tilde{S}k/\varepsilon$ and $C_2 = 1.9$.

The chemical source term $\dot{\omega}_k$ in Eq. (10) was obtained by the contribution of each of the N_R reactions as

$$\dot{\omega}_k = MW_k \sum_{j=1}^{N_R} (\nu_{k,j}^P - \nu_{k,j}^R) \left[k_{f,j} \prod_{s=1}^{N_s} \left(\frac{\rho Y_s}{MW_s} \right)^{\nu_{s,j}^R} - k_{b,j} \prod_{s=1}^{N_s} \left(\frac{\rho Y_s}{MW_s} \right)^{\nu_{s,j}^P} \right] \quad (18)$$

where MW_k denotes the molecular weight of species k. The generic reaction scheme among species M_k was expressed with stoichiometric coefficients of reactants $\nu_{k,j}^R$ and products $\nu_{k,j}^P$ as

$$\sum_{k=1}^{N_s} \nu_{k,j}^R M_k \leftrightarrows \sum_{k=1}^{N_s} \nu_{k,j}^P M_k \qquad (j = 1, \ldots, N_R) \quad (19)$$
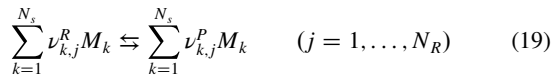
in which the forward and backward reaction rates were calculated by

$$k_{f,j} = A_j T^{n_j} \exp\left(-\frac{E_{a,j}}{\mathcal{R}T}\right) \qquad \text{and} \quad k_{b,j} = k_{f,j}/K_j \quad (20)$$

where $\mathcal{R}$ is the universal gas constant, A_j denotes the preexponential factor, n_j represents the temperature exponent, $E_{a,j}$ is the activation energy, and K_j stands for the equilibrium constant of the jth reaction obtained from thermodynamic data [34]. In the present work, a skeletal mechanism for ethylene oxidation consisting of 30 species and 143 reactions was employed. Furthermore, the eddy dissipation conception model [35] was exploited to handle the interaction between turbulence flow and chemical reaction, wherein the averaged source term $\bar{\dot{\omega}}_k$ was modeled as

$$\bar{\dot{\omega}}_k = -\frac{\bar{\rho}\gamma_\lambda^2}{\tau^*(1 - \gamma_\lambda^3)} (\tilde{Y}_k - Y_k^*) \quad (21)$$

$$\gamma_\lambda = C_\xi \left(\frac{\nu\varepsilon}{k^2}\right)^{1/4} \qquad \text{and} \quad \tau^* = C_\tau \left(\frac{\nu}{\varepsilon}\right)^{1/2} \quad (22)$$

in which γ_λ is the length fraction of the fine scale structure, τ^* is the reaction timescale, and Y_k^* is the mass fraction of species k after reaction at τ^*. C_ξ and C_τ are model constants that are taken as 2.1377 and 0.4083, respectively.

The structured mesh with boundary layers and local refinement was employed to model the HRE, and it is displayed in Fig. 3. Five topological similar meshes were generated to examine the grid convergence, which consisted of 10,401, 20,048, 40,916, 80,368, and 160,248 cells, respectively. The temperatures along the combustor centerline for these meshes are compared in Fig. 4a, which confirms that the spatial variation of temperature distribution was well resolved by all five grids. Taking the result obtained by the finest grid (160,248 cells) as the reference case, the relative errors in predicting the average chamber pressure $\varepsilon(\bar{p})$ are evaluated and displayed in a log–log style (Fig. 4b). The characteristic grid cell size h was calculated with the cross-sectional area A of the two-dimensional domain and the number of grid cells as $h = \sqrt{A/N}$. As can be observed, the relative error decreases as the mesh was refined. Consequently, the fine-level mesh comprising 80,386 cells was used in the subsequent modeling to balance the computational cost and accuracy. The boundary conditions included the mass flow inlet for propellant and ambient pressure at the pressure-outlet boundary together with non-slip and zero-species-flux conditions at the wall of the HRE.

The fully decomposed 90% H_2O_2 was assumed to generate a mixture comprising 42.35% oxygen and 57.65% water vapor at a temperature of 1013 K, whereas the paraffin was assumed to be a mixture of saturated alkanes that underwent a combustion process similar to that of ethylene (C_2H_4) [3]. For this reason, gaseous C_2H_4 at 800 K was used as the sole gas phase fuel reactant to simplify the calculations. Correspondingly, a 30-species 143-elemental-reaction skeletal mechanism was used for ethylene oxidation [36]. The convergence criteria were based on an absolute residual of 1×10^{-6} for all equations. To validate the numerical model employed in this study, the simulated chamber pressure was compared with the data obtained from the actual firing trial (case 15) and was found to be in good agreement (see Table 1). This concordance indicated that reliable simulation results were obtained in the present study.

III. Experimental Setup

Figure 5 provides a diagram of the experimental system used in this work, in which 90% H_2O_2 was employed as the oxidizer. The paraffin-based grain used as the solid fuel was formed by centrifugal casting and had a length of 75 mm [23]. An ethylene vinyl acetate copolymer was used as the adhesive to enhance the mechanical
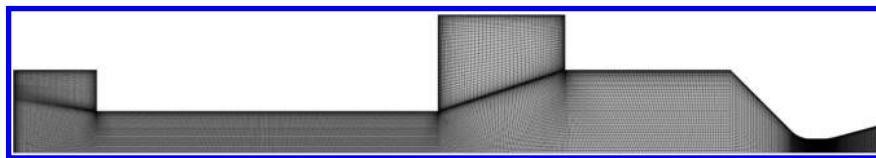

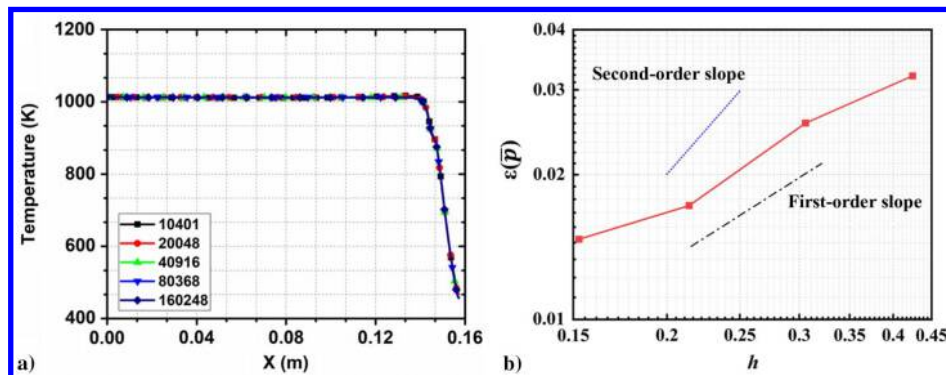**Fig. 3 Structural mesh for the two-dimensional HRE.**

Fig. 4 Representations of a) grid convergence in terms of temperature distribution along the combustor centerline, and b) combustor pressure and its relative error compared to the result obtained by the finest grid.

Table 1   Numerical validation

Method	P_c, MPa	T_{max}, K
Experiment	2.07	——
Rocket propulsion analysis	2.16	2714.0
Numerical simulation	2.16	2744.7
e, %	~4.3	~1.1

Table 2   Spectroscopic line parameters used in this work

Transition	Frequency ν_0, cm^{-1}	Line strength S, atm$^{-1} \cdot$ cm^{-2}	Low-state energy E'', cm^{-1}
1	7185.597	1.96×10^{-2}	1045.058
2	7444.35 + 7444.37 (combined)	1.10×10^{-3}	1774.751 1806.670

properties and melting point ($\approx$120°C) of the solid grain. For details of the fuel component, please refer to Ref. [21]. It is worth noting that the combustion chamber and nozzle were not installed during the H_2O_2 catalytic decomposition experiments but rather were only used in the catalytic ignition trials involving the HRE. In this system, the mass flow rate of H_2O_2 was adjusted using a flow controller (Bronkhorst, model M15) and a silver catalytic bed with a diameter of 20 mm was located at the head of the engine. The woven silver mesh was pressed to reduce the volume that it occupied while increasing the flow resistance and residence time. Ten layers of woven stainless-steel mesh were placed above and below the silver mesh layers, as shown in Fig. 6. This stainless-steel mesh was used to improve the dispersion effect and to provide support for the silver mesh at high temperatures. The axial injector with multiple straight ports was used downstream of the catalytic bed. Pressure transducers and thermocouples were situated both before and after the catalytic bed to monitor the working state of the bed.

The optical setup for the LAS system is also included in Fig. 5. In contrast to the thermocouple, which was positioned close to the catalyst bed outlet, the LAS measurements were performed along a plane intersecting the injector extension outlet to avoid shading of the laser by the thermocouple. Two distributed feedback (DFB) lasers (Nanoplus GmbH) were used, and the selected optimal transitions are

provided in Table 2. The injection current and temperature were adjusted using a diode-laser controller (Thorlabs ITC-502). Scanned wavelength direct absorption analyses were employed in this work [37]; and the incident laser was collimated using a collimating lens, with a focusing lens positioned before the first photodetector to enhance the signal. Two beam splitters were employed, and the two beams of reflected light were simultaneously sent through a room-temperature reference cavity and a Fabry–Perot interferometer to calibrate the absolute wavelength. The laser signals were simultaneously monitored by three InGaAs detectors (Thorlabs PDA10D), and the detector outputs were recorded at a sampling rate of 2.0 MHz.

IV.   Results and Discussion

A. H_2O_2 Decomposition in the Silver Catalytic Bed

The main results obtained from each group of H_2O_2 catalytic decomposition experiments and catalytic ignition experiments using the HRE are summarized in Table 3. The supply pressure of the oxidizer in each group was stable, and the mass flow rate ranged from 9.2 to 57 g/s.

The effect of preheating the catalytic bed on the H_2O_2 decomposition state was evaluated, and photographic images of these trials are presented in Fig. 7. The temperature of the preheated catalytic bed was relatively high, and so the temperature of the liquid H_2O_2
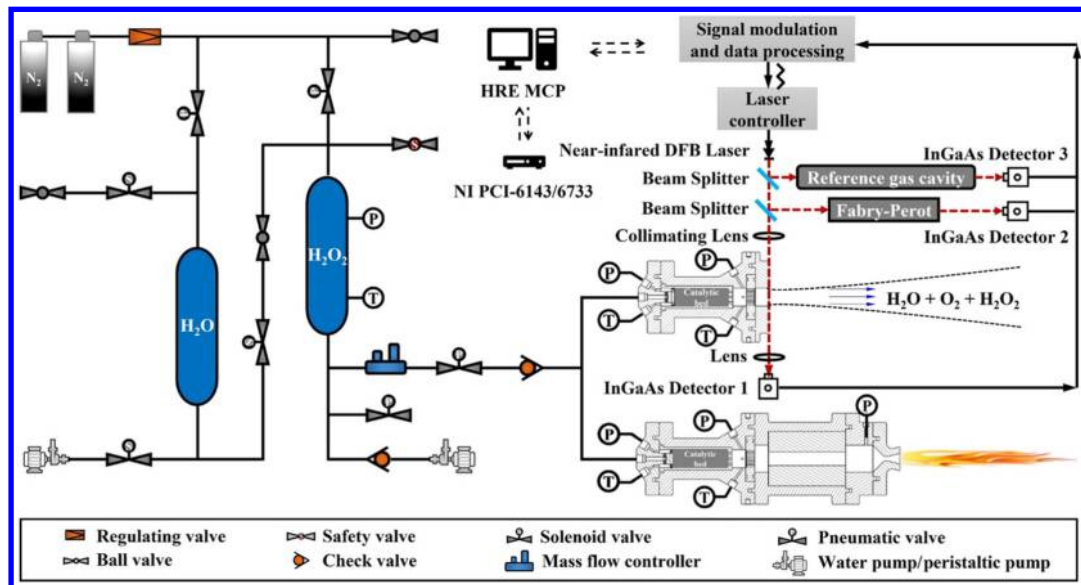
Fig. 5   Schematic diagram of the experimental setup together with the LAS system (MCP = Measurement and control program; NI = National instrument; P = Pressure; T = Temperature; LAS = Laser absorption spectrum).
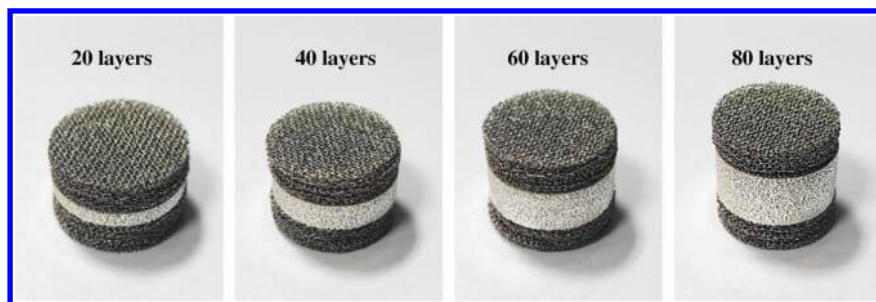
Fig. 6   Catalytic beds to be tested with different numbers of silver mesh layers.

Table 3 Summary of the catalytic decomposition experiments and firing tests

Case	Layer	T_{pre}, K	Ignition	t, s	$\dot{m}_{ox}$, g/s	T_{th}, K	O/F ratio	P_c, MPa
1	20	358	×	10	25.9	997	——	——
2	40	731	×	10	25.2	1005	——	——
3	60	365	×	10	24.2	1012	——	——
4	80	655	×	10	25.1	1001	——	——
5	60	275	×	10	57.0	366	——	——
6	60	374	×	10	34.3	1013	——	——
7	60	373	×	10	25.2	1004	——	——
8	60	384	×	10	21.5	988	——	——
9	60	750	×	10	17.4	1004	——	——
11	60	719	×	10	12.7	986	——	——
12	60	730	×	10	12.9	952	——	——
13	60	568	×	10	10.9	972	——	——
14	60	678	×	10	9.9	951	——	——
15	60	374	√	10	25.7	1013	4.3	2.1
16	60	560	×	3+3+3	19.9 + 17.3 + 13.0	678 + 947 + 957	——	——
17	60	362	√	3+3+3	32.9 + 31.3 + 30.1	647 + 941 + 952	5.1	2.4 + 2.5 + 2.5
18	60	672	√	3+3+3	27.6 + 25.0 + 23.1	782 + 927 + 938	4.9	2.1 + 2.0 + 1.9
e_m, %	——	≤0.3	——	≤3.3	≤1.0	≤1.2	≤0.5	≤0.5
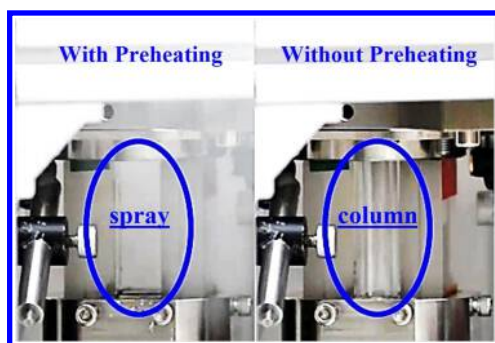
Fig. 7   Comparison of the catalytic decomposition states of H_2O_2 with and without preheating.

increased rapidly as it passed through the bed. In addition, the thermal expansion reduced the porosity of the catalytic bed, resulting in a prolonged residence time. Finally, the continuous decomposition of residual H_2O_2 in the catalytic bed during the preheating process provided a favorable initial condition for subsequent H_2O_2 decomposition, and so accelerated the decomposition rate. These images indicate that, in the absence of preheating, a large amount of liquid H_2O_2 was sprayed out in the shape of a column after passing through the spraying panel. This phenomenon would be extremely dangerous in actual engine applications because it would cause liquid accumulation in the combustion chamber, potentially leading to a very high ignition pressure peak or explosion. The corresponding temperature data are plotted in Fig. 8a and demonstrate that there was a minimal
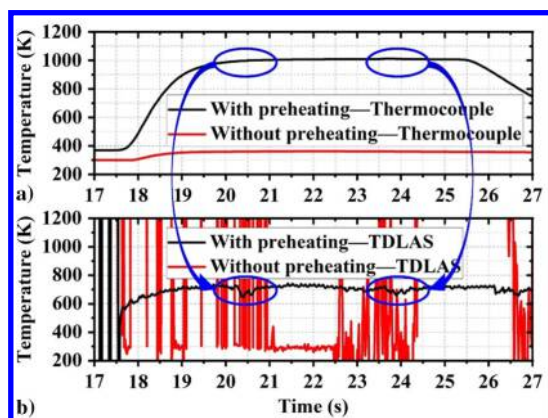
Fig. 8   Decomposition temperature data obtained with and without catalytic bed preheating using a) a thermocouple and b) the LAS system.

increase in the H_2O_2 decomposition temperature without catalytic bed preheating during the injection process because the liquid H_2O_2 continually absorbed heat from the bed.

Figure 8b plots the temperature data acquired using the LAS process following opening of the H_2O_2 supply valve at 17 s. Note that, as a result of the interference by the liquid decomposition components, the signal-to-noise ratio (SNR) was low during the initial stage of the trial. After the H_2O_2 underwent rapid decomposition for approximately 0.5 s, the flowfield no longer contained liquid components. Subsequent to this point, the SNR increased rapidly and the temperature simultaneously underwent a steep rise. At approximately 18.5 s, the temperature measured by the LAS system stabilized, whereas the values returned by the thermocouple indicated a stable decomposition temperature at approximately 20.5 s. The LAS data show several obvious fluctuations in the H_2O_2 decomposition temperature, primarily because of the autonomous adjustment of the flow controller. It should also be noted that refraction, reflection, and attenuation occurred when the laser light passed through the liquid H_2O_2 flowfield in the absence of preheating. The signal therefore displayed a low SNR such that it was difficult to ascertain the true temperature variations. The only period over which a useful signal was captured was from 21.0 to 22.5 s: during which, a low decomposition temperature of approximately 300 K was captured. These results indicate the viability of using LAS to rapidly assess the H_2O_2 decomposition state.

Figure 9a plots the time-resolved H_2O_2 decomposition temperatures obtained with different catalyst bed structures (that is, varying quantities of silver mesh layers) as obtained by LAS. The catalytic decomposition delay time, defined as the time required to reach 95% of the average decomposition temperature, gradually shortened with increases in the number of silver mesh layers up to 60 layers. This structure gave the shortest delay time of approximately 0.5 s. As the number of layers was further increased to 80, the delay time was extended to approximately 2.5 s based on the additional increase in the residence time. Figure 9b plots the average H_2O_2 decomposition temperatures as a function of the number of silver layers. The decomposition temperature is seen to have gradually increased up to a maximum of approximately 1013 K at 60 silver mesh layers. Further increases in the number of layers decreased the decomposition temperature based on the absorption of heat by the larger bed. It is also worth noting that the higher airflow velocity at the injector location resulted in lower-temperature values as compared with those returned by the thermocouple because the LAS data represent static temperature values. Nevertheless, the overall trend exhibited by the LAS data is consistent with that of the thermocouple values, demonstrating that LAS was a useful means of evaluating the performance of the catalytic bed.

The effect of the catalytic bed was not only affected by factors such as structure and preheating but also by the prolonged usage of the bed.
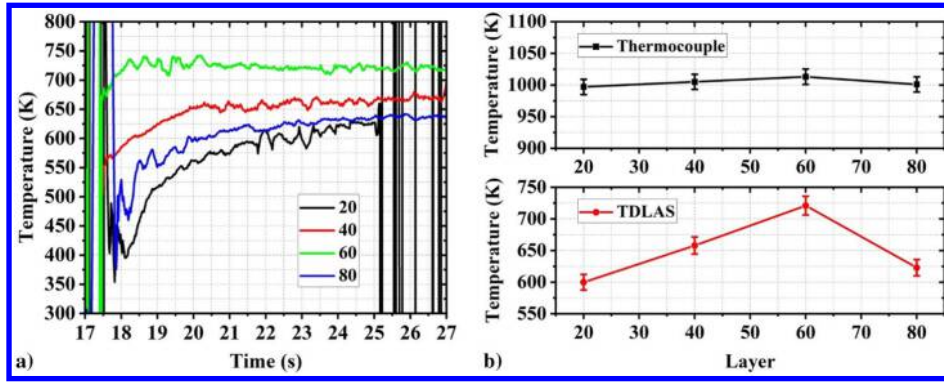
Fig. 9 Representations of a) temperatures of decomposition products as determined by LAS over time using varying quantities of silver layers in the catalytic bed, and b) average H_2O_2 decomposition temperatures as function of the number of silver mesh layers.
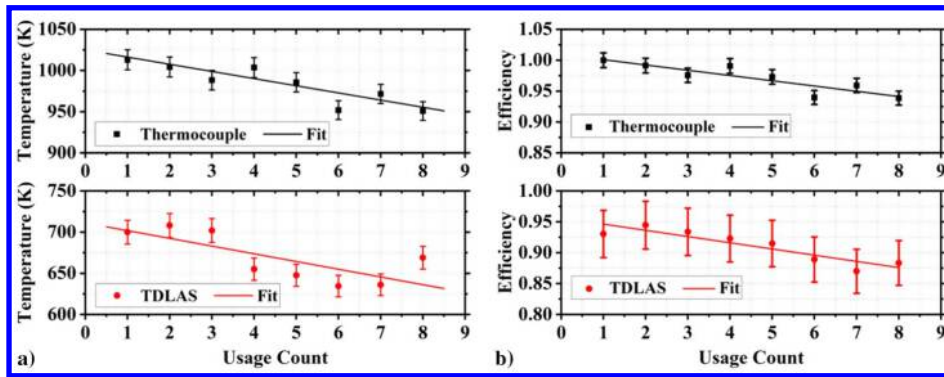

Fig. 10 Representations of a) average decomposition temperatures, and b) decomposition efficiencies obtained by the two measurement methods as a function of the number of times the catalyst bed was used.

Figure 10a presents the average decomposition temperatures obtained using a 60-layer silver mesh bed with preheating as a function of the number of times the catalytic bed was used. The trends shown by the thermocouple and LAS measurement results are consistent, and both indicate that the temperature gradually decreased with repeated usage. Based on Eqs. (9–11), the corresponding H_2O_2 decomposition efficiencies were obtained, and these values are shown in Fig. 10b. The plots obtained from the thermocouple and LAS data are very similar, although the LAS values are generally smaller. This may have occurred as a result of heat absorption as gaseous decomposition products flowed through the channel. Based on these plots, the decomposition efficiency of the silver catalytic bed in this work was calculated to decrease at a rate of approximately 0.0625%/s.

B. Effect of Decomposition Efficiency Decay on Combustion Characteristics

As the silver catalytic bed was reused, the catalytic decomposition efficiency decreased, which would be expected to change the combustion characteristics of the HRE. Case 15 (see Table 3) was selected as a reference to carry out numerical simulations of the HRE combustion process in conjunction with different decomposition efficiencies at a constant fuel mass flow rate of $\dot{m}_f \approx 6.0$ g/s. The decomposition products obtained at various decomposition efficiencies were determined by assuming that the mass flow rate of pure decomposed H_2O_2 was x g/s and the mass flow rate of pure undecomposed H_2O_2 was y g/s. On this basis, according to the conservation of mass, we can write

$$\frac{10(x+y)}{9} = \dot{m}_{ox} \tag{23}$$

Assuming that the catalytic decomposition of H_2O_2 occurred in a state of thermal equilibrium, meaning

$$Q_{d\_H_2O_2} = Q_{a\_H_2O_2} + Q_{a\_H_2O} + Q_{a\_O_2} \tag{24}$$

we have

$$\frac{xH_{D\_0}}{M_0} = \frac{yH_{V\_0}}{M_0} + \left(\frac{x+y}{9} + \frac{M_1}{M_0}x\right)\frac{H_{V\_1}}{M_1} + C_{P_0}(T_D - T_0)\dot{m}_0 + C_{P_1}(T_D - T_1)\dot{m}_1 + C_{P_2}(T_D - T_2)\dot{m}_2 \tag{25}$$

Equations (23) and (24) were used to calculate the mass flow rates of the decomposition products at 70, 80, 90, and 100% decomposition efficiencies, as shown in Table 4. The contours of the H_2O_2 and O_2 mass fractions for these different decomposition efficiencies are presented in Fig. 11 and indicate that the H_2O_2 concentration increased as the efficiency decreased. The H_2O_2 either decomposed or participated in the combustion reactions while moving along the grain channel. When the decomposition efficiency dropped to 80%, there was residual H_2O_2 at the nozzle outlet (shown in Fig. 11a). Also, the oxidizer was distributed radially in layers because structures or injection techniques that may have enhanced propellant mixing were not used in the present work. Figure 11b shows that the oxygen concentration near the fuel grain did not follow the trend of decreasing with the decomposition efficiency as in the core flow area, and it basically remains constant. This occurred primarily because the high temperature in the reaction zone accelerated the decomposition of H_2O_2. Figure 12 demonstrates that the OH concentration in this region was

Table 4   Mass flow rates of decomposition products associated with different decomposition efficiencies

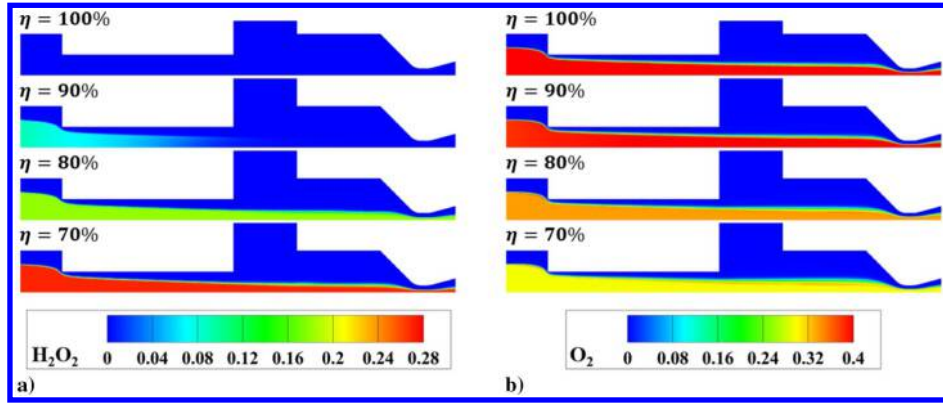| No	Efficiency, %	T/K	$\dot{m}_0$, g/s	$\dot{m}_1$, g/s	$\dot{m}_2$, g/s
1	100	1013	0	14.82	10.88
2	90	912	2.31	13.59	9.80
3	80	810	4.63	12.37	8.70
4	70	709	6.94	11.14	7.62

Fig. 11 Contours of a) H_2O_2 and b) O_2 mass fractions at different decomposition efficiencies.
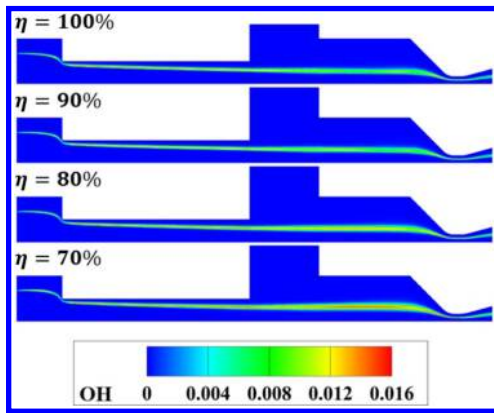

Fig. 12 Contours of OH mass fractions at different decomposition efficiencies.

relatively high, and this would be expected to effectively promote the reactions $OH + H_2O_2 \rightarrow H_2O + HO_2$ and $OH + HO_2 \rightarrow H_2O + O_2$.

Figure 13 shows the plots of the average pressure P_c and temperature T_c as a function of the decomposition efficiency. Both the average P_c and T_c show a similar downward trend as a decreasing η. When the η decreased to 90%, P_c and T_c decreased about 0.7 and 2.4%, respectively. This has little effect on the specific impulse of the engine (corresponding to the decrease of I_{sp} of about $1 \sim 2$ s). However, it is worth noting that there is an abrupt change in the decrease of both the P_c and T_c when the η drops to 80%. The average P_c and T_c decreased about 3.3 and 6.6% during this process, respectively, which corresponded to the I_{sp} drop of about $7 \sim 8$ s. The main reason is that part of the H_2O_2 was blown out of the combustion chamber without participating in the combustion and decomposition process, resulting in the decrease of P_c and T_c. Finally, when the η was reduced to 70%, the decrease of the average P_c and T_c slowed down again (0.7 and 1.8%, respectively), which corresponded to the decrease of I_{sp} of about $1 \sim 2$ s. During this process, the incompletely
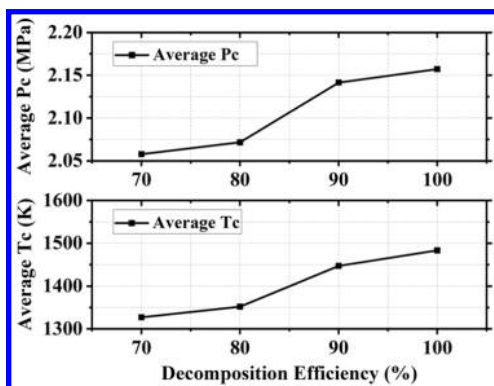
decomposed H_2O_2 continued to participate in the combustion and decomposition reactions to release heat, thereby slowing down the performance degradation rate caused by H_2O_2 mass loss.

C. Characteristics of Catalytic Ignition and Reignition

Catalytic ignition experiments using the H_2O_2/paraffin HRE were carried out to assess the performance of the silver catalytic bed. Figure 14 presents a series of photographic images showing the functioning of the laboratory-scale hybrid rocket, including catalytic decomposition, ignition, and flame development. During the catalytic decomposition stage, the temperature of the gas stream at the nozzle outlet gradually increased and the stream was transparent. The Mach barrel is also clearly visible at the nozzle outlet during the initial ignition stage. With the development of catalytic ignition, a bright flame appeared that remained stable as it grew. Variations in the combustion chamber pressure and the H_2O_2 tank pressure during the ignition phase are summarized in Fig. 15. The ignition delay time t_i can be divided into three stages comprising the valve response and pipeline filling time t_0, the catalytic decomposition delay time t_c, and the effective heating time Δt. The t_c value for H_2O_2 in the present work was less than 0.9 s, whereas t_i for the HRE was less than 1.4 s. If t_0 (≈ 0.4 s) is considered negligible because of the short transfer pipe and fast-response valve used in this apparatus, t_c and t_i will be shortened to 0.5 and 1 s, respectively. The data in Fig. 15b indicate that the valve response time t_1 and the pipeline filling time t_2 were approximately 0.25 and 0.15 s, respectively.

The reignition characteristics of the catalytic bed were further assessed by examining the rapidly repeated decomposition of H_2O_2 before the firing tests. Figure 16a shows a comparison of the decomposition temperatures obtained from the two measurement methods during three re-decomposition trials and demonstrates that the temperature data obtained from both the thermocouple and the LAS system continually and gradually increased during the first cycle P_1. The temperature returned by the thermocouple was approximately 860 K when the oxidizer supply was stopped at approximately 20 s, corresponding to a catalytic decomposition efficiency on the order of 85%, whereas the LAS temperature was 700 K. The latter value was equivalent to a decomposition efficiency of 97% according to Eq. (6) ($P_{x_{H_2O}} \approx 0.47$ atm, and $\overline{V}_g \approx 270$ m/s). The sudden drop in flow velocity caused the temperature measured by LAS to increase during the interval between the decomposition cycles. However, the temperature gradually decreased as the absorption of heat by the wall and heat losses caused by convection to the outside atmosphere occurred.

At approximately 22 s, the H_2O_2 supply valve was reopened. Figure 16b shows that the temperature measured by thermocouple and LAS showed a downward trend at the initial stage, which was caused by the entry of low-temperature hydrogen peroxide into the catalytic bed. Then, factors including the long response delay, short decomposition period, and heat losses caused the temperature measured by the thermocouple to continue to rise during this time span (close to 976 K at 25 s, and the decomposition efficiency obtained by thermocouple data on the order of 96%). However, the temperature characterized by LAS rose rapidly and remained stable after a short
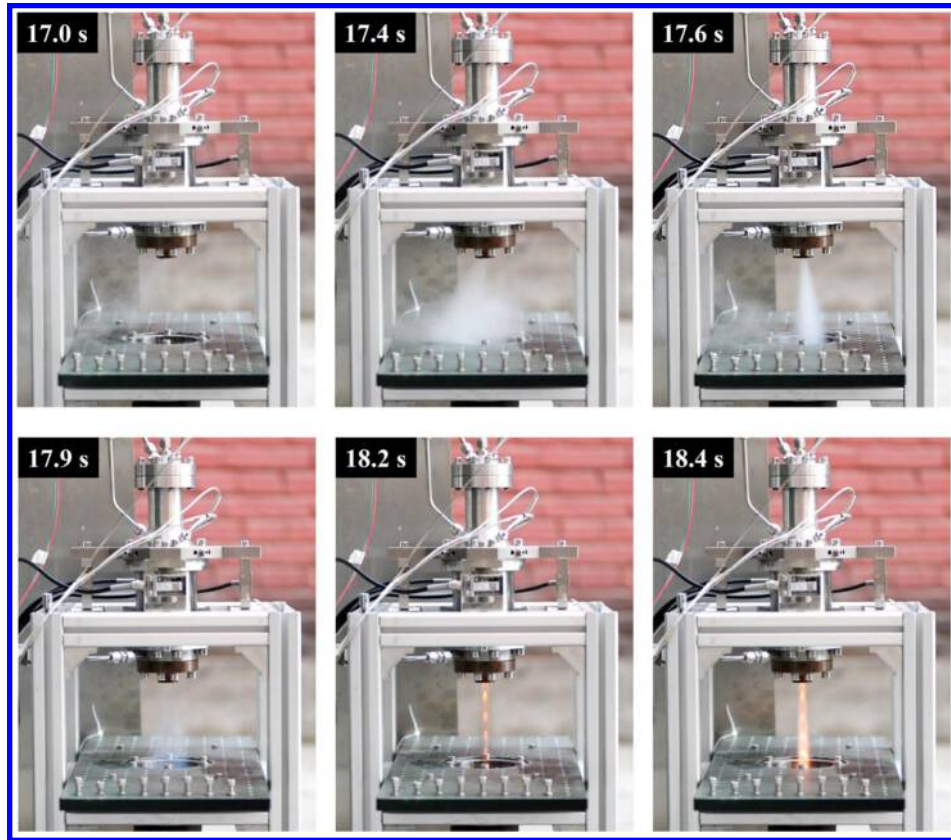

Fig. 13 Variations of average P_c and T_c with decomposition efficiency.

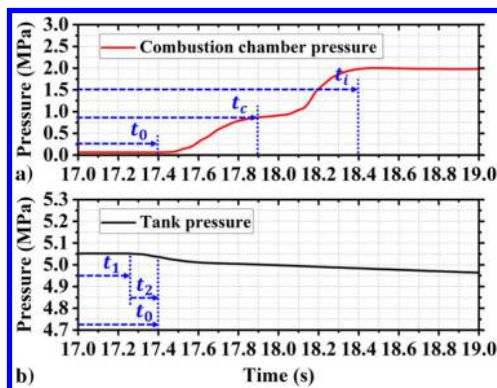**Fig. 14   Catalytic ignition of the H_2O_2/paraffin-based HRE.**

Fig. 15   Representations of a) combustion chamber pressure, and b) H_2O_2 supply pressure during ignition as the function of time.

time (≤ 0.25 s). The H_2O_2 decomposition efficiency calculated based on the LAS data remained essentially constant at approximately 105% during the second period P_2 ($P_{x_{H_2O}} \approx 0.46$ atm, and $\bar{V}_g \approx 255$ m/s). The preceding results significantly confirmed the advantages of LAS in the analysis of the rapid re-decomposition process of H_2O_2, which accurately provided the dynamic changes of parameters in the flow-field. The results obtained during period P_3 (from 27 to 30 s) were basically the same as those during P_2.

Finally, two sets of reignition experiments were performed using the HRE with different oxidizer mass flow rates to obtain additional data concerning the re-decomposition performance of the catalytic bed. Figure 17 shows the variation in both combustion chamber pressure and temperature as measured by the thermocouple. The ignition delay time of the paraffin-based fuel was evidently less than 1 s in all three working periods (including the initial catalytic ignition and the next two reignition processes). Due to the existence of
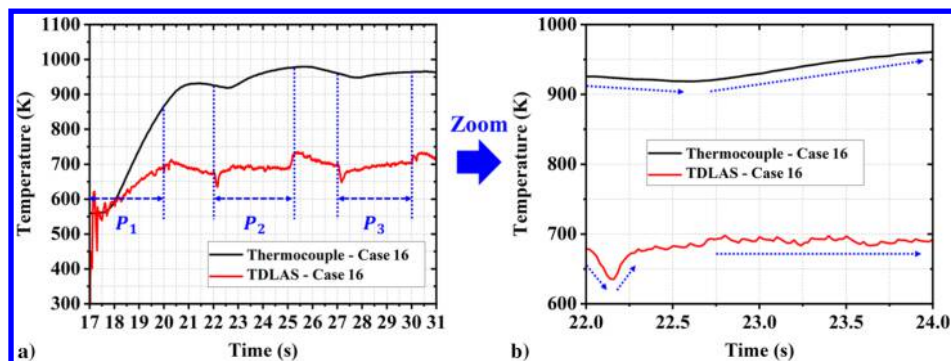

Fig. 16   Representations of a) temperature data acquired during rapid re-decomposition experiments as the function of time, and b) partial zoomed-in view of this process.
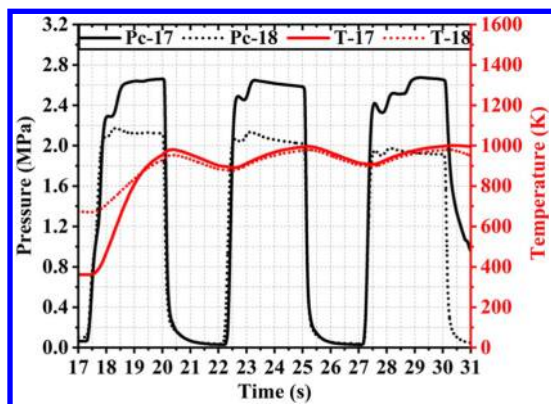
Fig. 17 Pressure and temperature data from tests involving rapid reignition of the HRE.

downstream backpressure, the flow velocity in the upstream chamber of the injector decreased, resulting in the maximum decomposition temperature of H_2O_2 reaching 1000 K. In addition, there were no obvious ignition pressure peaks in the last two periods, confirming that the rapid reignition of the paraffin-based fuel occurred regardless of the molten state of the inner wall of the grain.

These data indicate that a preheated silver catalytic bed with 60 layers of mesh provided suitable catalytic ignition and that the paraffin-based fuel could undergo rapid reignition. However, additional work is required to obtain a better understanding of the enhancement effect associated with decreased H_2O_2 decomposition efficiency. Additionally, the computational fluid dynamics model could be improved by taking heat transfer from the fuel into consideration. In future work, tunable diode-laser absorption tomography will be applied to determine the two-dimensional distributions of temperature and combustion products.

V. Conclusions

Experimental and numerical investigations concerning the catalytic ignition and combustion characteristics of a laboratory-scale HRE were conducted. Silver catalytic beds were assessed while monitoring the H_2O_2 decomposition temperature with a thermocouple, and an LAS system was used to provide comprehensive temperature data. The effects of preheating, the number of silver mesh layers, and the repeated reuse of the catalytic bed on the 90% H_2O_2 decomposition performance were clarified. Preheating of the catalytic bed was found to significantly increase the initial H_2O_2 decomposition rate, whereas increasing the number of silver mesh layers improved the decomposition efficiency. However, an excessive number of silver mesh layers and continuous catalytic bed reuse reduced the decomposition temperature because of heat losses and service life decay, respectively. The optimal performance was obtained with a preheated 60-layer bed, which gave a decomposition delay time of less than 0.5 s and a decomposition efficiency of 100%. The repeated reignition of this system gradually lowered the decomposition efficiency at a rate of approximately 0.0625%/s. The numerical simulation results showed that the engine performance decreased as the H_2O_2 decomposition efficiency decreased. When the H_2O_2 decomposition efficiency continued to drop to 80%, the engine performance decreased abruptly due to the mass loss of H_2O_2. Finally, firing tests were carried out with the optimal catalytic decomposition setup obtained from the preceding evaluation. Catalytic ignition of the H_2O_2/paraffin-based HRE was verified along with rapid reignition without pressure peaks.

Acknowledgments

References

[1] Schmierer, C., Kobald, M., Tomilin, K., Fischer, U., and Schlechtriem, S., "Low Cost Small-Satellite Access to Space Using Hybrid Rocket Propulsion," *Acta Astronautica*, Vol. 159, June 2019, pp. 578–583.
https://doi.org/10.1016/j.actaastro.2019.02.018

[2] Gieras, M., and Gorgeri, A., "Numerical Modelling of the Hybrid Rocket Engine Performance," *Propulsion and Power Research*, Vol. 10, No. 1, 2021, pp. 15–22.
https://doi.org/10.1016/j.jppr.2021.03.001

[3] Wang, Y., Hu, S., Liu, X., and Liu, L., "Regression Rate Modeling of HTPB/Paraffin Fuels in Hybrid Rocket Motor," *Aerospace Science and Technology*, Vol. 121, Feb. 2022, Paper 107324.
https://doi.org/10.1016/j.ast.2021.107324

[4] Guo, Z., Tian, H., Wang, Z., Meng, X., and Cai, G., "Numerical and Experimental Study on 95% Hydrogen Peroxide Catalytic Ignition of Hybrid Rocket Motors with HTPB-Based Aluminum Additive Fuel," *Acta Astronautica*, Vol. 195, June 2022, pp. 98–108.
https://doi.org/10.1016/j.actaastro.2022.03.004

[5] Ruffin, A., Paccagnella, E., Santi, M., Barato, F., and Pavarin, D., "Real-Time Deep Throttling Tests of a Hydrogen Peroxide Hybrid Rocket Motor," *Journal of Propulsion and Power*, Vol. 38, No. 5, 2022, pp. 833–848.
https://doi.org/10.2514/1.B38504

[6] Chiaverini, M., and Kuo, K., "Overview and History of Hybrid Rocket Propulsion," *Fundamentals of Hybrid Rocket Combustion and Propulsion*, Vol. 218, Progress in Astronautics and Aeronautics, edited by F. K. Lu, AIAA, Reston, VA, 2007, pp. 1–33.

[7] Tian, H., Li, X., and Cai, G., "Ignition Theory Investigation and Experimental Research on Hybrid Rocket Motor," *Aerospace Science and Technology*, Vol. 42, April 2015, pp. 334–341.
https://doi.org/10.1016/j.ast.2015.01.015

[8] Wei, S. S., Lee, M. C., Chien, Y. H., Chou, T. H., and Wu, J. S., "Experimental Investigation of the Effect of Nozzle Throat Diameter on the Performance of a Hybrid Rocket Motor with Swirling Injection of High-Concentration Hydrogen Peroxide," *Acta Astronautica*, Vol. 164, Nov. 2019, pp. 334–344.
https://doi.org/10.1016/j.actaastro.2019.07.020

[9] Jang, D., Kang, S., and Kwon, S., "Preheating Characteristics of H_2O_2 Monopropellant Thruster Using Manganese Oxide Catalyst," *Aerospace Science and Technology*, Vol. 41, Feb. 2015, pp. 24–27.
https://doi.org/10.1016/j.ast.2014.12.010

[10] Jo, S., "Response Characteristics of H_2O_2 Monopropellant Thrusters with Mno_2-Mixed Pbo Catalyst," *Aerospace Science and Technology*, Vol. 60, Jan. 2017, pp. 1–8.
https://doi.org/10.1016/j.ast.2016.10.022

[11] Connell, T. L., Risha, G. A., Yetter, R. A., and Natan, B., "Ignition of Hydrogen Peroxide with Gel Hydrocarbon Fuels," *Journal of Propulsion and Power*, Vol. 34, No. 1, 2018, pp. 170–181.
https://doi.org/10.2514/1.B36458

[12] John, J., Nandagopalan, P., Baek, S. W., and Cho, S. J., "Hypergolic Ignition Delay Studies of Solidified Ethanol Fuel with Hydrogen Peroxide for Hybrid Rockets," *Combustion and Flame*, Vol. 212, Feb. 2020, pp. 205–215.
https://doi.org/10.1016/j.combustflame.2019.10.029

[13] Yun, Y., Kim, J., and Kwon, S., "Parametric Study of Solid Fuel for Hydrogen Peroxide Hybrid Rocket Design," *Journal of Propulsion and Power*, Vol. 38, No. 2, 2022, pp. 229–240.
https://doi.org/10.2514/1.B38241

[14] Whitmore, S. A., Armstrong, I. W., Heiner, M. C., and Martinez, C. J., "High-Performing Hydrogen Peroxide Hybrid Rocket with 3-D Printed and Extruded ABS Fuel," AIAA Paper 2018-4443, July 2018.
https://doi.org/10.2514/6.2018-4443

[15] Cai, G., Li, C., Zhao, S., and Tian, H., "Transient Analysis on Ignition Process of Catalytic Hybrid Rocket Motor," *Aerospace Science and Technology*, Vol. 67, Aug. 2017, pp. 366–377.
https://doi.org/10.1016/j.ast.2017.03.041

[16] Tian, H., Yu, R., Zhu, H., Wu, J., and Cai, G., "Three-Dimensional Numerical and Experimental Studies on Transient Ignition of Hybrid Rocket Motor," *Acta Astronautica*, Vol. 140, Nov. 2017, pp. 247–254.
https://doi.org/10.1016/j.actaastro.2017.08.022

[17] Li, M. C., Wei, S. S., Hung, C. H., and Wu, J. S., "Experimental and Numerical Investigation of Swirling H_2O_2 and Polypropylene Hybrid Rocket Motor with Regenerative Cooling," *Acta Astronautica*, Vol. 190,

Jan. 2022, pp. 283–298.
https://doi.org/10.1016/j.actaastro.2021.09.026

[18] Karabeyoglu, M. A., Altman, D., and Cantwell, B. J., "Combustion of Liquefying Hybrid Propellants: Part 1, General Theory," *Journal of Propulsion and Power*, Vol. 18, No. 3, 2002, pp. 610–620.
https://doi.org/10.2514/2.5975

[19] Karabeyoglu, M. A., and Cantwell, B. J., "Combustion of Liquefying Hybrid Propellants: Part 2, Stability of Liquid Films," *Journal of Propulsion and Power*, Vol. 18, No. 3, 2002, pp. 621–630.
https://doi.org/10.2514/2.5976

[20] Adachi, M., and Shimada, T., "Liquid Films Instability Analysis of Liquefying Hybrid Rocket Fuels Under Supercritical Conditions," *AIAA Journal*, Vol. 53, No. 6, 2015, pp. 1578–1589.
https://doi.org/10.2514/1.J053459

[21] Wang, Z., Lin, X., Li, F., Zhang, Z., and Yu, X., "Improving the Combustion Performance of a Hybrid Rocket Engine Using a Novel Fuel Grain with a Nested Helical Structure," *Journal of Visualized Experiments*, Vol. 18, No. 167, 2021, Paper e61555.
https://doi.org/10.3791/61555

[22] Lin, X., Qu, D., Chen, X., Wang, Z., Luo, J., Meng, D., Liu, G., Zhang, K., Li, F., and Yu, X., "Three-Dimensional Printed Metal-Nested Composite Fuel Grains with Superior Mechanical and Combustion Properties," *Virtual and Physical Prototyping*, Vol. 17, No. 3, 2022, pp. 437–450.
https://doi.org/10.1080/17452759.2022.2035934

[23] Wang, Z., Lin, X., Li, F., and Yu, X., "Combustion Performance of a Novel Hybrid Rocket Fuel Grain with a Nested Helical Structure," *Aerospace Science and Technology*, Vol. 97, Feb. 2020, Paper 105613.
https://doi.org/10.1016/j.ast.2019.105613

[24] Zhang, Z., Lin, X., Wang, Z., Wu, K., Luo, J., Fang, S., Zhang, C., Li, F., and Yu, X., "Effects of Swirl Injection on the Combustion of a Novel Composite Hybrid Rocket Fuel Grain," *Acta Astronautica*, Vol. 199, Oct. 2022, pp. 174–182.
https://doi.org/10.1016/j.actaastro.2022.07.027

[25] Fang, S., Wang, Z., Lin, X., Li, F., Li, R., Li, J., Zhang, Z., Liu, Y., and Yu, X., "Characterizing Combustion of a Hybrid Rocket Using Laser Absorption Spectroscopy," *Experimental Thermal and Fluid Science*, Vol. 127, Sept. 2021, Paper 110411.
https://doi.org/10.1016/j.expthermflusci.2021.110411

[26] Wang, Z., Lin, X., Li, F., Peng, J., Liu, Y., Zhang, Z., Fang, S., and Yu, X., "Determining the Time-Resolved Mass Flow Rates of Hybrid Rocket Fuels Using Laser Absorption Spectroscopy," *Acta Astronautica*, Vol. 188, Nov. 2021, pp. 110–120.
https://doi.org/10.1016/j.actaastro.2021.07.028

[27] Li, R., Li, F., Lin, X., and Yu, X., "Error Analysis of Integrated Absorbance for TDLAS in a Nonuniform Flow Field," *Applied Sciences*, Vol. 11, No. 22, 2021, Paper 10936.
https://doi.org/10.3390/app112210936

[28] Li, R., Li, F., Lin, X., and Yu, X., "Linear Calibration-Free Wavelength Modulation Spectroscopy," *Microwave and Optical Technology Letters*, Oct. 2021.
https://doi.org/10.1002/mop.33063

[29] Lin, X., Chen, L. Z., Li, J. P., Li, F., and Yu, X. L., "Experimental and Numerical Study of Carbon-Dioxide Dissociation for Mars Atmospheric Entry," *Journal of Thermophysics and Heat Transfer*, Vol. 32, No. 2, 2018, pp. 503–513.
https://doi.org/10.2514/1.T5152

[30] Lin, X., Yu, X. L., Li, F., Zhang, S. H., Xin, J. G., and Chang, X. Y., "CO Concentration and Temperature Measurements in a Shock Tube for Martian Mixtures by Coupling OES and TDLAS," *Applied Physics B*, Vol. 110, No. 3, 2013, pp. 401–409.
https://doi.org/10.1007/s00340-012-5269-1

[31] Bird, R. B., Stewart, W. E., and Lightfoot, E. N., "Viscosity and the Mechanisms of Momentum Transport," *Transport Phenomena*, 2nd ed., Wiley, New York, 2002, pp. 11–40.

[32] Riedmann, H., Kniesner, B., Frey, M., and Munz, C. D., "Modeling of Combustion and Flow in a Single Element GH2/GO2 Combustor," *CEAS Space Journal*, Vol. 6, No. 1, 2014, pp. 47–59.
https://doi.org/10.1007/s12567-013-0056-3

[33] Shih, T.-H., Liou, W. W., Shabbir, A., Yang, Z., and Zhu, J., "A New k-ε Eddy Viscosity Model for High Reynolds Number Turbulent Flows," *Computers and Fluids*, Vol. 24, No. 3, 1995, pp. 227–238.
https://doi.org/10.1016/0045-7930(94)00032-T

[34] McBride, B. J., Zehe, M. J., and Gordon, S., "NASA Glenn Coefficients for Calculating Thermodynamic Properties of Individual Species," NASA TP-2002-211556, Sept. 2002.

[35] Magnussen, B., "On the Structure of Turbulence and a Generalized Eddy Dissipation Concept for Chemical Reaction in Turbulent Flow," AIAA Paper 1981-0042, Jan. 1981.
https://doi.org/10.2514/6.1981-42

[36] Wu, K., Yao, W., and Fan, X., "Development and Fidelity Evaluation of a Skeletal Ethylene Mechanism under Scramjet-Relevant Conditions," *Energy and Fuels*, Vol. 31, No. 12, 2017, pp. 14296–14305.
https://doi.org/10.1021/acs.energyfuels.7b03033

[37] Li, F., Yu, X., Gu, H., Li, Z., Zhao, Y., Ma, L., Chen, L., and Chang, X., "Simultaneous Measurements of Multiple Flow Parameters for Scramjet Characterization Using Tunable Diode-Laser Sensors," *Applied Optics*, Vol. 50, No. 36, 2011, pp. 6697–6707.
https://doi.org/10.1364/AO.50.006697

C. Segal
Associate Editor